Journal of Power Sources 195 (2010) 2659–2663

Contents lists available at ScienceDirect

Journal of Power Sources

journal homepage: www.elsevier.com/locate/jpowsour

Short communication

Y-doped $BaCeO_{3-\delta}$ nanopowders as proton-conducting electrolyte materials for ethane fuel cells to co-generate ethylene and electricity

Xian-Zhu Fu, Jing-Li Luo*, Alan R. Sanger, Nancy Luo, Karl T. Chuang

Department of Chemical and Materials Engineering, University of Alberta, Edmonton, Alberta T6G 2G6, Canada

ARTICLE INFO

Article history:
Received 16 July 2009
Received in revised form 22 October 2009
Accepted 27 October 2009
Available online 1 November 2009

Keywords:
Doped barium cerate
Perovskite
Nanopowders
Proton-conducting electrolyte
Solid oxide fuel cell
Ethane dehydrogenation to ethylene

ABSTRACT

Y-doped $BaCeO_{3-\delta}$ (BCY) powders synthesized using a combustion method are pure perovskite phases. The particles are uniform spherical particles about 50 nm. The properties of BCY proton-conducting electrolyte sintered at different temperatures from pressed nanopowders were systematically investigated. Dense BCY pellets are obtained at temperatures higher than 1400 °C for 10 h. Electrical conductivity and resistance to CO_2 atmosphere each increase with sintering temperature. Fuel cells having about 0.8 mm thick BCY electrolyte and Pt electrodes co-produce 151 mW cm^{-2} electrical power and value-added ethylene with selectivity over 90% at ethane conversion about 35% at 700 °C.

1. Introduction

Proton-conducting oxides have received considerable attentions as potential electrolyte materials for solid oxide fuel cells (SOFCs) in recent years [1–7]. Compared with conventional SOFCs using oxygen ion electrolytes, those with proton-conducting electrolyte have unique advantages. For example, water is produced at the cathode, thus avoiding fuel dilution at the anode. Especially, value-added alkenes can be co-generated with electricity and without greenhouse gas (CO_2) emission when alkanes such as ethane and propane are used as fuels [8–11]. Among the proton-conducting electrolyte materials for SOFCs, Y-doped $BaCeO_{3-\delta}$ (BCY) perovskite oxides have been intensively investigated due to their excellent proton conductivity at intermediate temperature [12–17].

The reported BCY powders were prepared mostly using conventional solid state reactions since the processes are simple and cost-effective. However, using these reactions it is difficult to obtain super-fine ceramic powders with homogeneous composition, uniform shape and size because of poor raw materials dispersion by physical mixing and relatively high sintering temperature for phase formation [18,19]. Dense electrolyte with excellent properties can be easier to obtain by sintering uniform nanopowders when compared with the use of irregular micrometer sized powders [20,21]. Furthermore, very thin electrolyte film can be readily fabricated from nanopowders [22]. However, there are few reports about barium cerate based perovskite nanopowders as electrolyte materials for SOFCs [18,21,23], in particular for hydrocarbon SOFCs to generate value-added alkenes.

In this paper, we describe synthesis of BCY nanopowders, their structure and properties as proton-conducting electrolyte sintered at different temperatures, and performance of ethane SOFCs using BCY proton-conducting electrolyte to co-produce ethylene and electricity.

2. Experimental

2.1. Sample preparation and characterization

15% Y-doped $BaCeO_{3-\delta}$ ($BaCe_{0.85}Y_{0.15}O_{3-\delta}$) nanopowders were prepared by a citric acid–nitrate combustion method. Stoichiometric amounts of $Ba(NO_3)_2$, $Ce(NO_3)_3{\cdot}6H_2O$ and $Y(NO_3)_3{\cdot}6H_2O$ salts were first dissolved in deionized water. Subsequently, citric acid as chelating agent and NH_4NO_3 as oxidant agent were added (the molar ratio of citric acid:total metal ions:NH_4NO_3 was 1.5:1:3). The resulting solution was adjusted to pH 8 with ammonium hydroxide and heated on a hot plate to evaporate water until it changed into brown foam and then ignited. After combustion, the obtained ash was calcined at 900 °C in air for 5 h to obtain BCY powders.

BCY electrolyte pellets were prepared by pressing the BCY nanopowders at 5 tonnes in a 2.54 cm diameter die and sintering

* Corresponding author. Tel.: +1 780 492 2232; fax: +1 780 492 2881.
E-mail address: Jingli.Luo@ualberta.ca (J.-L. Luo).

0378-7753/$ – see front matter © 2009 Elsevier B.V. All rights reserved.
doi:10.1016/j.jpowsour.2009.10.069

subsequently at different temperatures for 10 h. Platinum paste was placed on each side of the sintered discs to form 0.28 cm^2 electrodes, then they were heated at 900 °C for 30 min to obtain membrane electrode assemblies (MEA) ready for conductivity measurement and fuel cell fabrication.

The phase structures of materials were identified using a Rigaku Rotaflex X-ray diffractometer (XRD) with Co Kα radiation. The shapes and particle sizes of powders were determined using a Philips Morgagni 268 transmission electron microscope (TEM). The density of each sintered BCY disc was calculated directly from their weights and volumes after sintering. Morphologies of sintered BCY disc surfaces were determined using a Hitachi S-2700 scanning electron microscope (SEM).

The chemical stability of sintered BCY electrolytes in CO_2 atmosphere was determined using a TA SDT Q600 thermal gravity analysis (TGA) in a CO_2/He flow (CO_2 = 15 mL min^{-1}; He = 100 mL min^{-1}) from room temperature to 1200 °C at a heating rate of 10 °C min^{-1}.

The conductivity of BCY electrolyte was measured in 10% H_2 (balance with He) humidified gas using a.c. impedance spectroscopy in the frequency range from 0.1 Hz to 10^6 Hz. A Solartron 1287 electrochemical interface together with 1255B frequency response analysis instrumentation was used for all electrochemical tests.

2.2. Fuel cell system fabrication and tests

The fuel cell was set up by securing the MEA between coaxial pairs of alumina tubes (the internal diameter of the outer alumina tubes was 8 mm) and sealed using ceramic sealant (Aremco 503), which was cured by heating in a vertical Thermolyne F79300 tubular furnace. The heating rate of the furnace was 1 °C min^{-1}. Ethane and oxygen were used as anode and cathode gas, respectively.

The outlet gases from the anode chamber were analyzed using a Hewlett-Packard model HP5890 GC equipped with a packed bed column (OD: 1/8 IN; length: 2 m; Porapak QS) operated at 80 °C with thermal conductivity detector. The ethane conversion and ethylene selectivity were calculated according to the previously reported method [8].

3. Results and discussion

3.1. Characterization of BCY nanopowders

The combusted powders after calcination at 900 °C was pure perovskite phase (XRD, Fig. 1), and matched file data PDF#01-071-6752 for $BaCe_{0.85}Y_{0.15}O_{3-\delta}$. This result showed that the perovskite phase of BCY could be obtained at lower temperatures via combustion method relative to the conventional solid state reaction synthesis which usually exploits temperatures more than 1000 °C [24]. The metal ions were dissolved into the solution and chelated with citric acid that led to homogeneous distribution of the elements and thereby enabled ready formation of perovskite phase. The BCY powders consisted of spherical particles with average diameter about 50 nm (TEM, Fig. 2). During the combustion process, a large amount of gas emanated from the reaction of NH_4NO_3 and the homogenously mixed metal citric acid complex gel, resulting in formation of very small sized particles of BCY precursor oxide. However, physical aggregation of nanopowders was noted after calcination at 900 °C due to cosintering of nanoparticles.

3.2. Properties of sintered BCY electrolyte

Densities of BCY discs remarkably depended on the sintering temperature (Fig. 3). Density exponentially increased with sintering temperature from 70% to 96% of the theoretical value

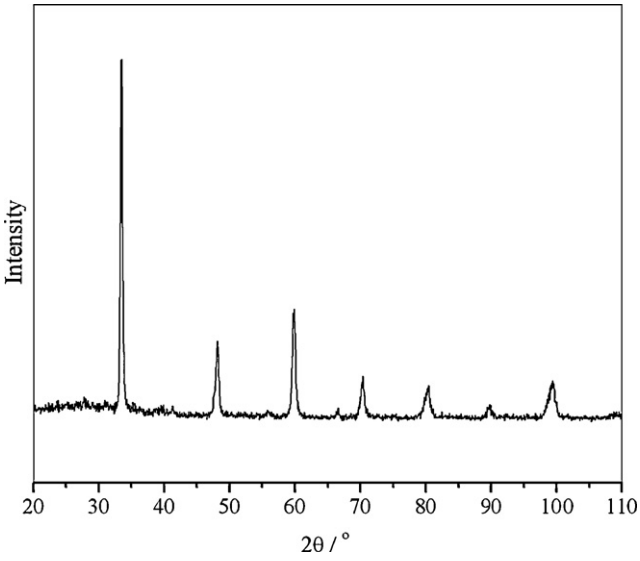

Fig. 1. XRD patterns of calcined BCY powders prepared by combustion method.

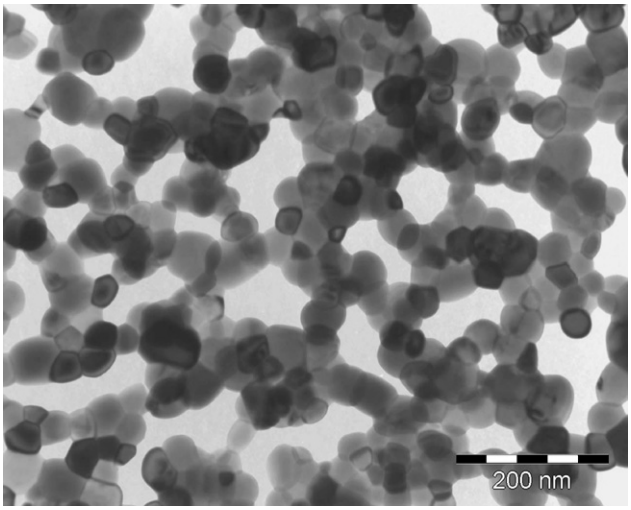

Fig. 2. TEM images of calcined BCY powders prepared by combustion method.

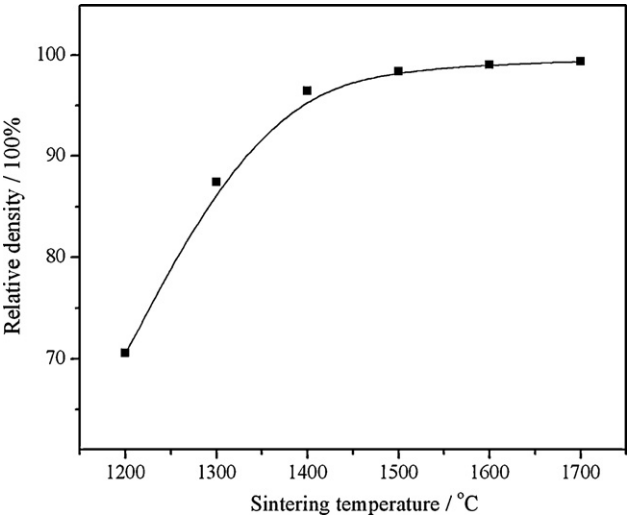

Fig. 3. Density of BCY discs as a function of sintering temperature.

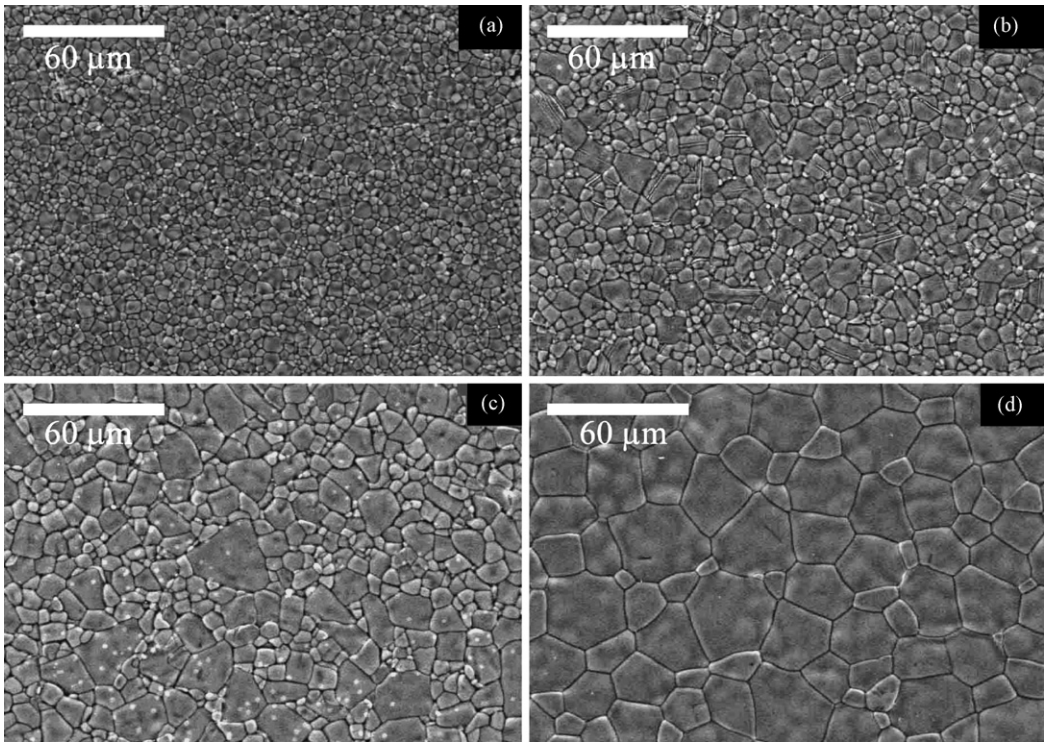

Fig. 4. Surface SEM images of BCY discs sintered at different temperatures for 10 h: (a) 1400 °C; (b) 1500 °C; (c) 1600 °C; and (d) 1700 °C.

as the temperature increased from 1200 °C to 1700 °C. Dense BCY discs were formed when sintered at 1400 °C for 10 h (SEM, Fig. 4a). Thus, BCY nanopowders could be sintered well within 10 h at the relatively low temperature of 1400 °C to form dense structure, which was attributed to the very small particle size and uniform shape of BCY powders. The average sintered grain size was about 3 μm, which was much larger than that of the original (calcined) BCY nanopowders. The average grain size of BCY became larger as the sintering temperature increased, about 40 μm at 1700 °C (Fig. 4). XRD patterns (Fig. 5) displayed sharper BCY perovskite phase diffraction peaks as the sintering temperature increased, showing that the BCY became more crystalline at higher sintering temperature, which was consistent with the SEM data.

The XRD data showed an additional characteristic derived from the low temperature sintering procedure that only applied to the nanopowders described herein. In contrast to material sintered at relatively low temperatures, there were weak $Ce_{1-x}Y_xO_2$ diffraction peaks (PDF# 083-0326) in the XRD patterns of BCY sintered at 1600 °C and 1700 °C due to ceria formed on the BCY surface as a result of BaO vaporization at high sintering temperatures above 1500 °C [25,26]. However, the impurity did not form in detectable amounts during low temperature sintering, and so the electrolyte was substantially pure BCY.

It is well known that BCY readily reacts with CO_2 at elevated temperature, with the consequence that the pervoskite structure

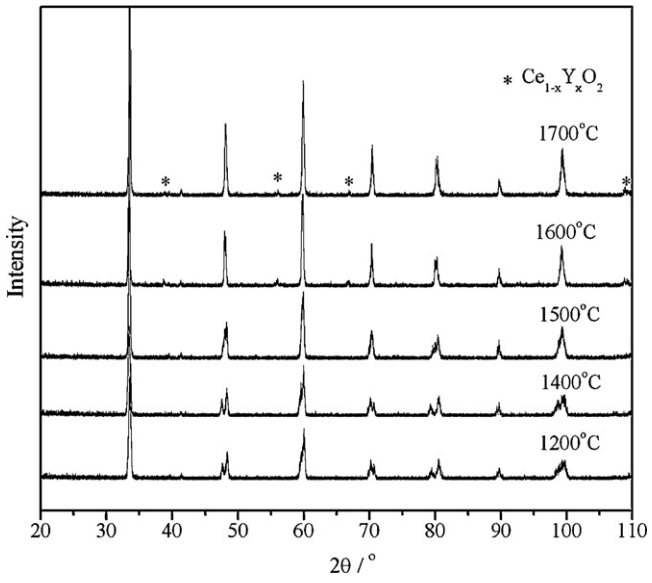

Fig. 5. XRD patterns of BCY discs sintered at different temperatures for 10 h.

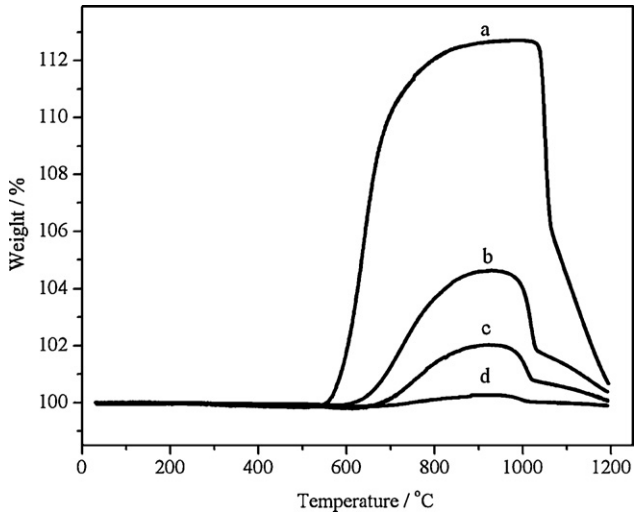

Fig. 6. TGA curves in CO_2 atmosphere for BCY sintered at different temperatures: (a) 1400 °C; (b) 1500 °C; (c) 1600 °C; and (d) 1700 °C.

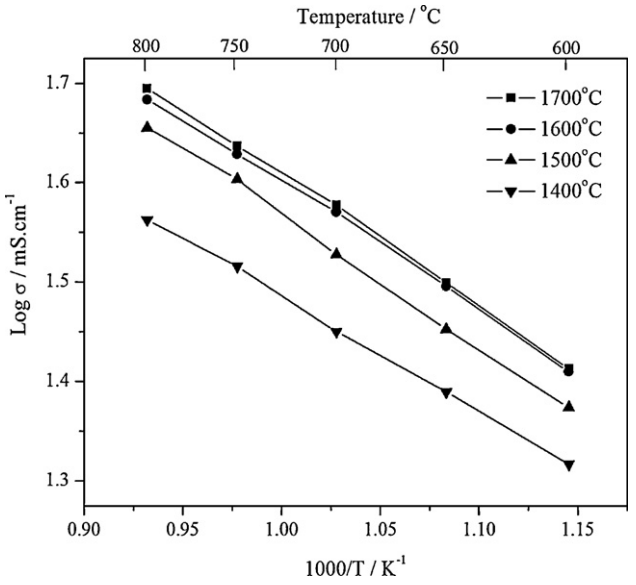

Fig. 7. BCY conductivity at 600–800 °C in humid hydrogen atmosphere (10% H_2, balance with He).

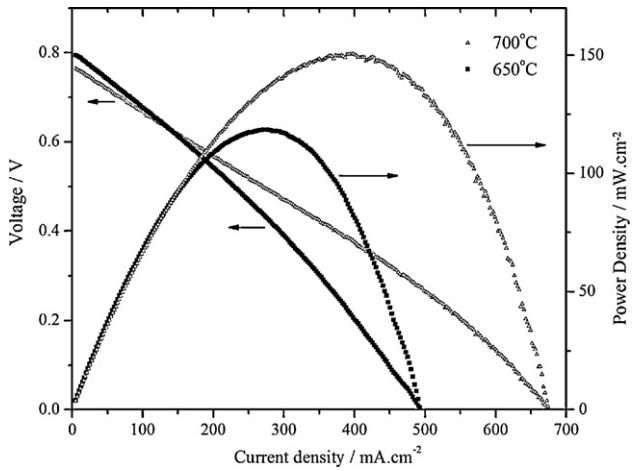

Fig. 8. Current density–voltage and power density curves of ethane/oxygen fuel. Cells at 650 °C and 700 °C. The thickness of BCY electrolyte is about 0.8 mm. The flow rates of ethane and oxygen are 100 mL min^{-1}.

becomes increasingly unstable. This reaction causes deterioration over time of the performance of hydrocarbon or syngas fuel cells using BCY electrolyte [27]. The chemical stability in CO_2 atmosphere of BCY formed by sintering nanopowder was evaluated using TGA in a stream of CO_2/He. There was almost no weight change below about 550 °C (Fig. 6), and then there was strong weight uptake above that temperature up to a maximum value of 12.7% for BCY sintered at 1400 °C, associated with the reaction of BCY with CO_2. As the temperature increased further the weight then sharply declined above a temperature about 1000 °C, as $BaCO_3$ decomposed to BaO and CO_2, and BCY was re-formed by reaction of BaO with CeO_2 at the higher temperature, similar to the previously reported results [24]. Thus, the presented results confirmed chemical instability of BCY in CO_2 atmosphere. It should be noted that amount of the weight uptake by reaction of CO_2 with BCY decreased markedly with the sintering temperature of BCY, and the onset temperature for weight uptake peak increased. In particular, the weight uptake of BCY sintered at 1700 °C was much lower. The observed decrease of the weight uptake of BCY samples sintered at higher temperatures can be attributed to their higher density and ceria rich surface. This property will be of value in operation of ethane fueled proton-conducting SOFCs with enhanced resistance to CO_2 atmosphere.

The total conductivities in humidified hydrogen of BCY electrolyte sintered at different temperatures increased with temperature in the range 600–800 °C (Fig. 7). At any given test temperature, the total conductivity of BCY electrolyte increased as the sintering temperature increased from 1400 °C to 1700 °C. The increase in conductivity with sintering temperature was attributed to increase in the grain size and concomitant grain boundary resistance reduction, leading to improved BCY ionic conductivity.

3.3. Performance of ethane fuel cell with BCY electrolyte

Electrolyte prepared with BCY nanopowders sintered at 1700 °C exhibited the best conductivity and CO_2 chemical resistance, and so it was used to fabricate ethane fuel cells with Pt electrodes. The anode and cathode feeds were dry ethane and oxygen, respectively, each at 100 mL min^{-1}.

At elevated temperatures, ethane was catalytically dehydrogenated to ethylene at the anode. The produced protons were conducted through BCY electrolyte to the cathode where they reacted with oxygen ions to form water. At 650 °C, the maximum power density of the fuel cell was 118 mW cm^{-2} at current density 276 mA cm^{-2} (Fig. 8). The corresponding ethylene selectivity was 95.2% at 22.7% ethane conversion, and the major by-product was methane. Carbon oxides were formed in trace amounts, possibly by reaction provided by minor transference of oxygen ions through electrolyte membrane. At 700 °C, the maximum power density of the fuel cell increased to 151 mW cm^{-2} at current density 393 mA cm^{-2}, with ethane conversion enhanced to 35.1%. However, ethylene selectivity decreased to 91.6% and selectivity to methane increased. Increased conversion to methane at higher temperatures suggested that it arose from cracking of ethane, in competition with ethane dehydrogenation. Increasing the discharging current density, the conversion of ethane increased, as the rate of proton removal from the anode increased (Fig. 9). In addition, the ethane conversion change is higher at 700 °C than 650 °C at the same current density, showing that electrochemical dehydrogenation was enhanced relative to chemical dehydrogenation at the higher temperature.

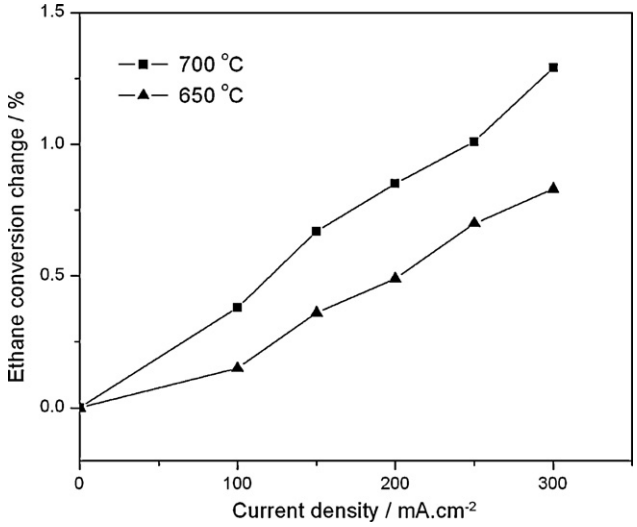

Fig. 9. Change in ethane conversion with increase in current density at 650 °C and 700 °C. The flow rates of ethane and oxygen each are 100 mL min^{-1}.

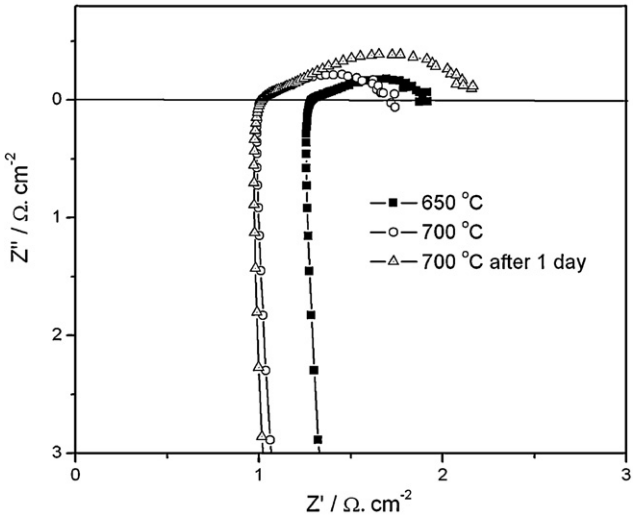

Fig. 10. Electrochemical impedance spectra (EIS) of ethane/oxygen fuel cell with BCY electrolyte and Pt electrodes at 650 °C and 700 °C. The flow rates of ethane and oxygen each are 100 mL min^{-1}.

The electrochemical impedance spectra (EIS) of the dry ethane fueled fuel cell under open circuit conditions is shown in Fig. 10. The intercepts with the real axis at high frequency and the succeeding semi-circle, assigned to electrolyte ohmic and electrode polarization resistances, respectively. The electrolyte resistances of dry ethane fueled fuel cell were smaller than those calculated from the data in Fig. 7 which were measured in humidified hydrogen atmosphere. It might result from the enhancement of electronic conduction in the BCY electrolyte due to the dry and reduced gas of ethane in the anode [28], which also was confirmed by open circuit voltages (OCVs) analysis. The measured OCVs of the ethane fuel cell were 0.80 V and 0.77 V at 650 °C and 700 °C, respectively. They were about 0.2 V lower than the theoretical OCVs (0.99 V at 650 °C and 0.98 V at 700 °C) for the electrochemical dehydrogenation of ethane (Eq. (1)).

$$C_2H_6\ (g) + \frac{1}{2}O_2\,(g) = C_2H_4\,(g) + H_2O\,(g) \quad (1)$$

Fig. 10 shows that there was no apparent change in ohmic resistance over 24 h, though the electrode polarization resistance increased. The result showed that the BCY electrolyte was stable, however the Pt electrode degenerated during the 24 h test. Although Pt is an excellent dehydrogenation catalyst and electrical conductor, it is readily poisoned by deposition of carbon derived from ethane [9]. Furthermore, Pt is expensive and very unlikely by used in practical solid oxide fuel cells. More stable and lower cost electrode catalyst will be developed.

Compared to conventional oxidative conversion of ethane to ethylene [29,30], the ethylene selectivity in the proton-conducting solid oxide fuel cell was higher, the process was simpler, and chemical energy was recovered as high grade electrical power. Importantly, there were no detectable amounts of acetylene in the anode effluent, which is a serious issue for manufacture of ethylene for use in polymerization processes: acetylene poisons several classes of polymerization catalysts, in particular Ziegler–Natta and metallocene types of catalyst [31]. Therefore, there were advantages of ethane SOFC resulting from use of a proton-conducting electrolyte: (1) there was no exposure of ethane and product ethylene to any oxidative reagents or oxygen ions which might form from oxygen ion electrolyte; (2) protons generated at the anode were removed rapidly through the proton-conducting electrolyte, which separated the electrode reactions, and therefore the ethane conversion reaction was not equilibrium limited; and (3) the electrochemical process generated high grade electrical energy mainly via the reaction of protons and oxygen ions.

4. Conclusions

About 50 nm particle size $BaCe_{0.85}Y_{0.15}O_{3-\delta}$ (BCY) spherical powders were synthesized by a modified citric acid–nitrate combustion method. Dense BCY pellets were obtained by sintering these at more than 1400 °C for 10 h. The conductivity and CO_2 chemical resistance of BCY electrolyte increased with increasing sintering temperature. A solid oxide fuel cell with BCY electrolyte and Pt electrodes demonstrated 91.6% ethylene selectivity at 35.1% ethane conversion with cogeneration of 151 mW cm^{-2} power output at 700 °C.

Acknowledgements

This work was supported by Natural Sciences and Engineering Research Council of Canada/NOVA Chemicals CRD Grant and the Alberta Energy Research Institute. The authors also would like to thank Mrs. Weizhu An for her help in GC and TGA measurements as well as Dr. Juri Melnik and Dr. Andrzej Krzywicki for very helpful discussions.

References

[1] H. Iwahara, Solid State Ionics 77 (1995) 289–298.
[2] C.D. Zuo, S.W. Zha, M.L. Liu, M. Hatano, M. Uchiyama, Adv. Mater. 18 (2006) 3318–3320.
[3] K. Xie, Q.L. Ma, B. Lin, X.Q. Liu, G.Y. Meng, J. Power Sources 170 (2007) 38–41.
[4] E. Fabbri, A. D'Epifanio, E. Di Bartolomeo, S. Licoccia, E. Traversa, Solid State Ionics 179 (2008) 558–564.
[5] L. Bi, S. Zhang, S. Fang, Z. Tao, R. Peng, W. Liu, Electrochem. Commun. 10 (2008) 1598–1601.
[6] B. Lin, Y. Dong, R. Yan, S. Zhang, M. Hu, Y. Zhou, G. Meng, J. Power Sources 186 (2009) 446–449.
[7] Y. Guo, Y. Lin, R. Ran, Z. Shao, J. Power Sources 193 (2009) 400–407.
[8] S.Y. Wang, J.L. Luo, A.R. Sanger, K.T. Chuang, J. Phys. Chem. C 111 (2007) 5069–5074.
[9] Z.C. Shi, J.L. Luo, S.Y. Wang, A.R. Sanger, K.T. Chuang, J. Power Sources 176 (2008) 122–127.
[10] Y. Feng, J.L. Luo, K.T. Chuang, J. Power Sources 167 (2007) 486–490.
[11] Y. Feng, J.L. Luo, K.T. Chuang, J. Phys. Chem. C 112 (2008) 9943–9949.
[12] A.N. Virkar, H.S. Maiti, J. Power Sources 14 (1985) 295–303.
[13] T. Hibino, A. Hashimoto, M. Suzuki, M. Sano, Electrochem. J. Soc. 149 (2002) A1503–A1508.
[14] A. Longo, F. Giannici, A. Balerna, C. Ingrao, F. Deganello, A. Martorana, Chem. Mater. 18 (2006) 5782–5788.
[15] W. Suksamai, I.S. Metcalfe, Solid State Ionics 178 (2007) 627–634.
[16] N. Maffei, L. Pelletier, A. McFarlan, J. Power Sources 175 (2008) 221–225.
[17] E. Gorbova, V. Maragou, D. Medvedev, A. Demin, P. Tsiakaras, J. Power Sources 181 (2008) 207–213.
[18] D.W. Lee, J.H. Won, K.B. Shim, Mater. Lett. 57 (2003) 3346–3351.
[19] B. Meng, X.Y. Tan, B.Y. Zhang, N.T. Yang, Rare Metals 25 (2006) 79–83.
[20] E.R. Trejo, J.S. Salazar, R.V. Morales, A.B. Rico, F.G. García, C.F. Morales, J.C. Carvayar, G. Tavizón, J. Solid State Chem. 180 (2007) 3093–3100.
[21] G. Chiodelli, L. Malavasi, C. Tealdi, S. Barison, M. Battagliarin, L. Doubova, Fabrizio, C. Mortalò, R. Gerbasi, J. Alloys Compd. 470 (2009) 477–485.
[22] X.S. Xin, Z. Lu, Q.S. Zhu, X.Q. Huang, W.H. Su, J. Mater. Chem. 185 (2007) 1627–1630.
[23] S. Barison, M. Battagliarin, T. Cavallin, L. Doubova, M. Fabrizio, C. Mortalo, S. Boldrini, L. Malavasi, R. Gerbasi, J. Mater. Chem. 18 (2008) 5120–5128.
[24] R.C.T. Slade, N. Singh, Solid State Ionics 61 (1993) 111–114.
[25] D. Hirabayashi, A. Tomita, S. Teranishi, T. Hibino, M. Sano, Solid State Ionics 176 (2005) 881–887.
[26] A. Tomita, K. Tsunekawa, T. Hibino, S. Teranishi, Y. Tachi, M. Sano, Solid State Ionics 177 (2006) 2951–2956.
[27] K. Katahira, Y. Kohchi, T. Shimura, H. Iwahara, Solid State Ionics 138 (2000) 91–98.
[28] D. Hirabayashi, A. Tomita, M.E. Brito, T. Hibino, U. Harada, M. Nagao, M. Sano, Solid State Ionics 168 (2004) 23–29.
[29] A.S. Bodke, D.A. Olschki, L.D. Schmidt, E. Ranzi, Science 285 (1999) 712–715.
[30] D.W. Flick, M.C. Huff, J. Catal. 178 (1998) 315–327.
[31] Y. Azizi, C. Petit, V. Pitchon, J. Catal. 256 (2008) 338–344.